

# Spherical probes at ion saturation in $\mathbf{E} \wedge \mathbf{B}$ fields

Leonardo Patacchini and Ian H. Hutchinson

Plasma Science and Fusion Center, MIT

## Abstract

The ion saturation current to a spherical probe in the entire range of ion magnetization is computed with SCEPTIC3D, new three-dimensional version of the kinetic code SCEPTIC designed to study transverse plasma flows. Results are compared with prior two-dimensional calculations valid in the magnetic-free regime [I.H. Hutchinson PPCF 44:1953 (2002)], and with recent semi-analytic solutions to the strongly magnetized transverse Mach probe problem [L. Patacchini and I.H. Hutchinson PRE ???]. At intermediate magnetization (ion Larmor radius close to the probe radius) the plasma density profiles show a complex three-dimensional structure that SCEPTIC3D can fully resolve, and contrary to intuition the ion current peaks provided the ion temperature is low enough. Our results are conveniently condensed in a single factor  $M_c$ , function of ion temperature and magnetic field only, providing the theoretical calibration for a transverse Mach probe with four electrodes placed at  $45^\circ$  to the magnetic field in a plane of flow and magnetic field.

## 1 Introduction

Despite the continuous development of novel plasma diagnostic techniques seen in the past decades [1], achieving a fine monitoring of rotation profiles in magnetic fusion devices is still an area of active investigation. The effort is in particular motivated by the need to understand edge sheared flows, thought to reduce turbulence in tokamaks and facilitate the transition from L to H confinement mode [2, 3].

Transverse Mach probes are part of the toolbox for measuring plasma fluid velocities close to the separatrix and in the Scrape Off Layer (SOL) [4, 5], where ions drift towards the diverter plates at a substantial fraction of the sound speed. Their operation is simple in concept: by comparing the ion saturation flux-density  $\Gamma_i$  at different angles in the plane of flow and magnetic field, one seeks to measure the external, or unperturbed (intended as in the absence of probe) plasma drift velocity  $\mathbf{v}_d$ . The most promising probe design is perhaps the so-called Gundestrup [6], characterized by a set of (at least 3) different electrodes spanning the tip of a single insulating head. Because it can also operate as an array of Langmuir probes [1, 7, 8] and measure basic quantities such as temperature, density and potential, the transverse Mach probe became a polyvalent, quasi-routine diagnostic, now starting to be installed in hardly accessible regions such as the high-field side of Alcator C-mod [9].

Electrodes inserted in a plasma impart a localized perturbation to the ion and electron populations, and most of the challenge yet to overcome lies in developing a model of current collection relating measurements to the plasma properties at infinity. This is a long-standing problem of considerable complexity, relevant not only to probe physics but also to the charging of dust [10]

and spacecraft [11], as well as to the physics of magnetospheric flows around moons [12]. In typical conditions relevant to probe experiments, the electron Debye length  $\Lambda_{De}$  is much shorter than any other relevant scale length, in particular the probe size  $R_p$  and the average ion Larmor radius  $R_L$ . Provided the bias voltage is negative enough, an infinitesimal Debye sheath forms at the probe surface and the ion current saturates; the plasma region requiring treatment is then quasineutral. Furthermore, integration of the electron momentum balance along the magnetic field lines directly relates the density to the local electrostatic potential through a Boltzmann law, effectively transforming the electrostatic force acting on the ions into an additional pressure gradient.

In the strong magnetization limit, when the average ion Larmor radius is much smaller than the probe dimensions but larger than the Debye length:  $\Lambda_{De} \ll R_L \ll R_p$ , the dynamic is one-dimensional outside the so called magnetic presheath, layer a few  $R_L$ s thick in the cross-field direction where the Larmor motion is broken and the ions are accelerated towards the Debye sheath. Collisionless one-dimensional isothermal fluid calculations [13] then yield convenient analytic expressions for the ion saturation flux-density; in the downstream region for instance ( $\eta \in [0 : \pi]$ )

$$\begin{aligned} \Gamma_{i\parallel}(\eta) &= N_\infty c_{sI} \exp[-1 - (M_\infty - M_\perp \cot \eta)] & \text{when } M_\infty - M_\perp \cot \eta \geq -1 \\ \Gamma_{i\parallel}(\eta) &= -N_\infty c_{sI} (M_\infty - M_\perp \cot \eta) & \text{when } M_\infty - M_\perp \cot \eta < -1, \end{aligned} \quad (1)$$

where  $M_\infty = v_\infty/c_{sI}$  and  $M_\perp = v_\perp/c_{sI}$  are the parallel and transverse external Mach numbers,  $c_{sI}$  the unperturbed isothermal ion sound speed (Eq. (5)) and  $\eta$  the angle between the magnetic field and the probe tangent in the plane of field and drift. The ion saturation flux-density  $\Gamma_{i\parallel}$  is intended as charge per unit time per unit surface perpendicular to the magnetic field, hence needs to be multiplied by the projection of the local probe normal on the magnetic field  $|\mathbf{e}_r \cdot \mathbf{B}/B|$  to obtain the ion saturation flux per unit probe surface,  $\Gamma_i$ . The upstream equivalent of Eq. (1) is readily obtained upon replacing  $\eta$  by  $\pi - \eta$  and  $M_\infty$  by  $-M_\infty$ . Extension of the theory accounting for the full parallel ion distribution function [14] provides “exact” semi-analytic solutions to the Mach probe problem in the strong magnetization limit. The geometry is illustrated in Fig. (1) for a spherical probe.

In the regime of intermediate magnetization, the dynamics can not be treated as one-dimensional and the ion saturation current *a priori* depends on the full probe shape rather than only the angle  $\eta$  at the point of measurement. This paper reports three-dimensional Particle In Cell (PIC) simulations of collisionless ion collection by a non emitting spherical probe at saturation, in uniform background magnetic and convective electric fields  $\mathbf{B}$  and  $\mathbf{E}_{\text{conv}}$  enforcing a plasma “ $\mathbf{E} \wedge \mathbf{B}$ ” drift. The unperturbed plasma is taken as uniform, thus excluding diamagnetic drifts arising from transverse pressure gradients. The probe radius  $R_p$  is much larger than  $\Lambda_{De}$ , justifying a quasineutral treatment, but can take any value with respect to  $R_L$ . For this purpose we use the new tool SCEPTIC3D, derived from the 2D3v code SCEPTIC [15, 16] and described in section 2. We then proceed with the results concerning the plasma profiles (Section 3), the ion saturation fluxes and a proposed Mach probe calibration methodology (Section 4).

## 2 Model and computational method

### 2.1 Problem formulation

We consider a uniform, fully ionized Maxwellian plasma of monoionized ions (charge  $Z$ ) and electrons, characterized by charge density  $ZN_i = N_e = N_\infty$  and temperatures  $T_{i\infty}$  and  $T_e$ . The plasma

(a) Three-dimensional view

(b) Two-dimensional cross-section

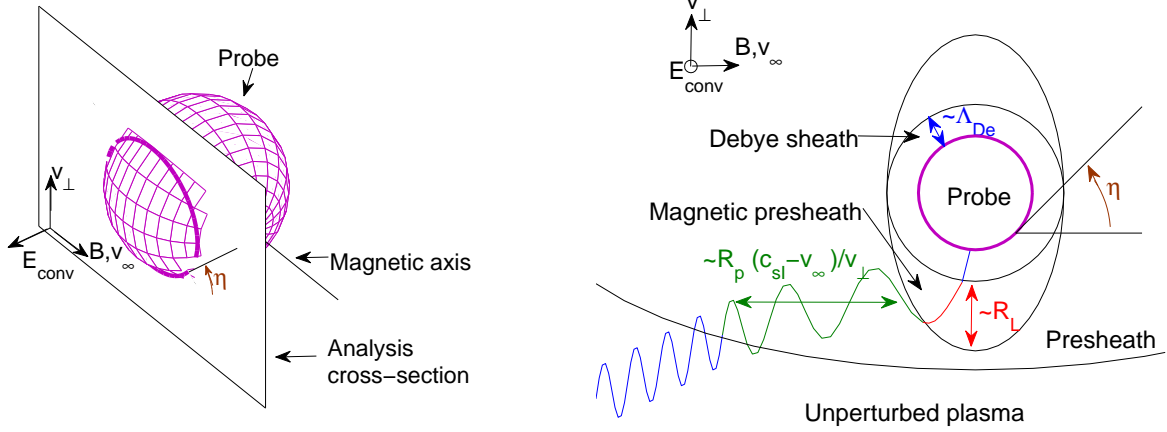


Figure 1: (a) Geometry of the spherical Mach probe problem in the  $\Lambda_{De} \ll R_L \ll R_p$  scaling, considering a purely convective drift. (b) A “typical” collected ion starts in the upstream unperturbed plasma, drifting with cross-field velocity  $\mathbf{v}_\perp$ . It first sees the probe when entering the presheath, where it is accelerated along  $\mathbf{B}$  over a length  $\sim R_p(c_{sI} - v_\infty)/v_\perp$  (for subsonic flows) while still drifting in the cross-field direction. This one-dimensional dynamics breaks in the magnetic presheath as the ion accelerates radially towards the non neutral Debye sheath.

has an external drift  $\mathbf{v}_d = \mathbf{v}_\perp + \mathbf{v}_\infty$ , respectively cross-field and parallel velocities to a uniform background magnetic field  $\mathbf{B}$ . The ion and electron populations as well as the electrostatic potential  $\Phi$  are perturbed by a perfectly absorbing spherical probe of radius  $R_p$  located at the origin. The cross-field drift is driven by an external convective field  $\mathbf{E}_{\text{conv}}$ :  $\mathbf{v}_\perp = (\mathbf{E}_{\text{conv}} \wedge \mathbf{B})/B^2$ , hence the total electric field at a given point in space is  $\mathbf{E} = \mathbf{E}_{\text{conv}} - \nabla\Phi$ .

The electron Debye length  $\Lambda_{De} = (\epsilon_0 T_e / e^2 N_\infty)^{1/2}$  is infinitesimal with respect to  $R_p$  and the average ion Larmor radius at infinity

$$R_L = \frac{1}{ZeB} \left( \frac{\pi m T_{i\infty}}{2} \right)^{1/2}, \quad (2)$$

hence Poisson’s equation for the potential can be replaced by quasineutrality  $ZN_i = N_e$ , as long as the probe bias is negative enough for a Debye sheath to form at its surface. Further approximating the electrons as massless, their momentum equation can easily be integrated along the magnetic lines upon neglecting the acceleration term. The procedure yields isothermal electrons with Boltzmann density, down to a distance of the order the electron Larmor radius from the probe surface:  $N_e = N_\infty \exp(e\Phi/T_e)$  [17]. Each ion, of mass  $m$  and position  $\mathbf{x} = (x, y, z)^T$ , is governed by Newton’s equation

$$\frac{m}{Ze} \frac{d^2 \mathbf{x}}{dt^2} = \mathbf{E}_{\text{conv}} - \nabla\Phi + \frac{d\mathbf{x}}{dt} \wedge \mathbf{B}. \quad (3)$$

Sample plasma parameters for the mid-plane SOL of a DD C-Mod tokamak discharge are  $T_e = 10eV$ ,  $T_{i\infty} = 30eV$ ,  $B = 5T$  and  $N_{i,e} = 10^{18}m^{-3}$  [18], yielding  $\Lambda_{De} = 23\mu m$  and  $R_L = 200\mu m$ , while typical probes are millimeter sized.

For convenience, distances are measured in unit of probe radius, potential  $\phi$  in  $T_e/e$ , velocity in the cold-ion sound speed

$$c_{s0} = \left( \frac{ZT_e}{m} \right)^{1/2}, \quad (4)$$

time  $t$  in  $R_p/c_{s0}$ , and charge density in  $N_\infty$ . Dimensionless distances and densities are indicated by low-case characters. We also define Mach numbers “ $M$ ” intended as velocity divided by isothermal ion sound speed

$$c_{sI} = \left( \frac{ZT_e + T_{i\infty}}{m} \right)^{1/2}, \quad (5)$$

the temperature ratio at infinity  $\tau = T_{i\infty}/ZT_e$ , and the magnetic field strength as the ratio of the probe radius to the mean ion Larmor radius at infinity  $\beta_i = R_p/R_L$ :

$$\beta_i = ZeBR_p \left( \frac{2}{\pi m T_{i\infty}} \right)^{1/2}. \quad (6)$$

Charge flux-densities are naturally in units of  $N_\infty c_{s0}$ . However for easy comparison with previous treatments we will scale them either to the random thermal charge flux-density

$$\Gamma_i^0 = N_\infty \frac{v_{ti}}{2\sqrt{\pi}}, \quad (7)$$

where  $v_{ti} = (2T_{i\infty}/m)^{1/2}$  is the ion thermal speed, or to the isothermal sound flux  $N_\infty c_{sI}$ . The random thermal current to the sphere is defined by  $I_i^0 = 4\pi R_p^2 \Gamma_i^0$ .

## 2.2 Code Operation

We solve the problem using the newly developed hybrid PIC code SCEPTIC3D, whose structure is mostly derived from SCEPTIC [15].

The probe is embedded in a spherical computational domain of radius  $r_b$ , subdivided in cells parameterized by spherical coordinates  $(r, \theta, \psi)$ , and uniformly spaced in  $r$ ,  $\cos \theta$  and  $\psi$ . The first and last radial centers are located at  $r = 1$  and  $r = r_b$ , and the first and last polar centers at  $\cos \theta = \pm 1$ ; the corresponding cells are hence “half cells”. We arbitrarily define  $\mathbf{e}_z$  as the magnetic axis, and  $\mathbf{e}_y$  such that  $\mathbf{v}_d$  is in the  $\{\mathbf{e}_y, \mathbf{e}_z\}$  plane,  $\delta$  being the angle between  $\mathbf{B}$  and  $\mathbf{v}_d$ . The computational domain is sketched in Fig. (2).

At each time-step, charge density is linearly extrapolated to the cell centers from a set of  $n_{\text{part}}$  computational ions spanning the domain (Cloud in cell approach). The electrostatic potential, straightforwardly given by quasineutrality

$$\phi = \ln(n), \quad (8)$$

is then differentiated on the grid and interpolated back to each ion, which can then be advanced according to Eq. (3). We mention here that a parallelized Poisson solver has also been implemented in SCEPTIC3D, in order to investigate finite Debye length plasmas where quasineutrality does not apply. Code operation in this regime is deferred to future work.

The  $n_{\text{part}}$  particles representing ions are advanced in Cartesian coordinates using the Cyclotronic integration scheme [19], in the frame moving with velocity  $\mathbf{v}_\perp$  where  $\mathbf{E}_{\text{conv}}$  vanishes. This enables

(a) Three-dimensional view

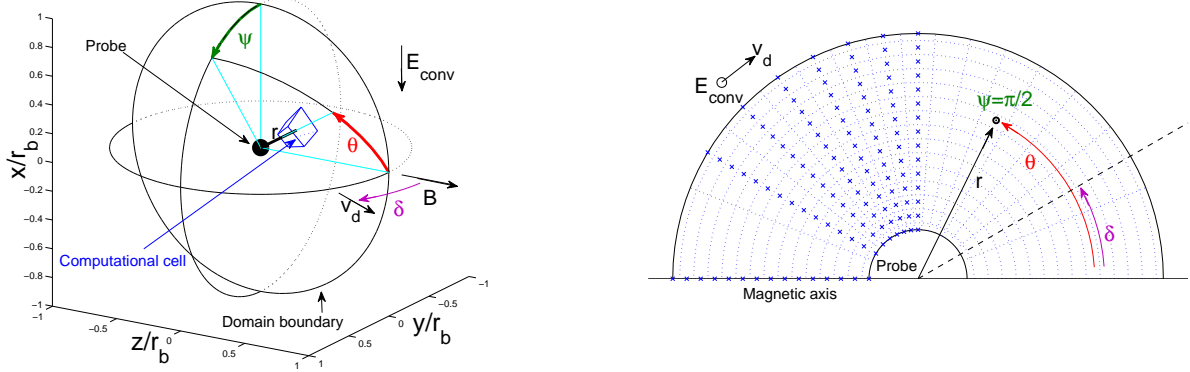
(b)  $\psi = \pi/2$  cross-section

Figure 2: (a) Three-dimensional view of the computational domain. (b) Cross-section at  $\psi = \pi/2$ , half plane containing the drift velocity  $\mathbf{v}_d$ . Computational cell centers for  $\cos \theta \leq 0$  are indicated by “x”-symbols.

us to use longer time-steps as the strong convective acceleration need not be resolved. In order to increase the accuracy at which orbit-probe intersections are computed, integration is subcycled in the probe vicinity. This procedure breaks symplecticity, but because no orbit is periodic or quasi-periodic we shall not be concerned about this minor effect.

### 2.3 Boundary Conditions

The total number of computational ions in the domain is fixed, therefore when an ion leaves the domain (by colliding with the probe or by crossing the outer boundary) it is randomly reinjected at the outer boundary. The probability distribution of position and velocity is chosen consistent with the ions being Maxwellian with temperature  $T_{i\infty}$  and drift velocity  $\mathbf{v}_d$ .

Of course the downstream region is perturbed by the probe, and the ion distribution function there is far from Maxwellian. Unless we run the code with an excessively large computational domain, plasma profiles close to the downstream outer boundary are therefore biased by our reinjection scheme. Because information can not propagate against the cross-field drift (at least on a scale longer than the average ion Larmor radius), a moderate uncertainty on the downstream potential distribution will however not affect the upstream dynamics. The saturation current will therefore be correct provided each ion collected by the probe entered the computational domain from an unperturbed plasma region. This condition is met for large enough computational domains, qualitatively:

$$r_b \gtrsim \frac{2}{M_{\perp}}. \quad (9)$$

In the simulation, each computational ion is given equal weight such that the *upstream* normalized charge density is unity.

The inner boundary in our quasineutral formulation is really the Debye sheath entrance rather than the probe surface, although geometrically the two are degenerate. The potential at  $r = 1$  is

therefore still given by quasineutrality and the probe bias voltage is irrelevant. Because the potential gradient at the sheath edge has a square root singularity, it is not possible to correctly extrapolate the density there from the grid, and in Ref. [15] the sheath entrance potential was self-consistently adjusted so as to enforce Bohm condition. In SCEPTIC3D we adopt a different approach, where the sheath entrance density (hence potential) is calculated by dividing the dimensional probe flux-density by the average radial velocity of the ions crossing the inner boundary.

A further consequence of the square root singularity is that the potential gradient can not properly be linearly interpolated in  $r$  from the grid to the ions, at least in the sheath neighborhood. For this reason we follow Ref. [15], where the interpolation is performed in an alternative radial coordinate proportional to the square root of the distance from the sheath edge  $\zeta = \sqrt{2(r-1)}$ ; the radial gradient is then  $\partial\phi/\partial r = (\partial\phi/\partial\zeta)/\zeta$ . This is one of the major advantages of using a mesh isomorphic to the probe, and it is unlikely that a code with unstructured mesh or immersed-boundary probe treatment can achieve the same order accuracy.

## 2.4 Accuracy

The code is “embarrassingly” parallelized by assigning a subset of  $n_{\text{part}}$  to each of  $n_{\text{proc}}$  processors, typically  $n_{\text{proc}} = 128$  and  $n_{\text{part}}/n_{\text{proc}} = 400k$ . The simulation starts with uniform ion density, and runs past convergence. Code outputs such as density or current densities are then averaged over the last 25% of the steps, yielding smooth solutions suitable to further postprocessing and analysis.

Regardless of the number of time-steps over which the averaging is performed, we must ensure that the “raw” outputs are unaffected by the discretization of phase-space. In our quasineutral simulations, the Debye length is much smaller than any computational cell. Charge fluctuations due to the usage of a finite number of particles are therefore  $Q \propto 1/\sqrt{n_{\text{cell}}}$ , where  $n_{\text{cell}}$  is the typical number of particles per cell; at radius  $r$ ,  $n_{\text{cell}} \simeq n_{\text{part}}r^2/(4/3\pi r_b^2 n_r n_\theta n_\psi)$ . Inner cells being the smallest, noise will first affect the region close to the probe where ions mostly have a radial motion. We can therefore assume that potential fluctuations deflect the ions similarly to Coulomb collisions with cross-section  $\sigma \propto Q^2/(n_\theta n_\psi)$ , yielding an effective dimensionless computational mean-free-path scaling as

$$l = \frac{n_{\text{part}}}{n_\theta n_\psi n_r^2 r_b}. \quad (10)$$

Fig. (3) shows the total ion saturation current  $I_i$  to the probe as a function of  $1/l$  (varied by changing the number of particles and modifying the grid), for the plasma parameters  $\tau = 0.1$ ,  $v_d = 0.5c_{s0}$ ,  $\delta = \pi/4$ , and  $\beta_i = 1$ . It can be seen that if we aim at noise levels of the order 1%, we need to operate with  $l \gtrsim 1$ ; this is a rather general observation, holding not only for the selected case but for most plasma parameters. In fact the higher the ion temperature, the lower the effect of potential fluctuations.

The impression that the output does not depend on the grid coarseness when  $l \gtrsim 1$  is however misleading. First we are looking at  $I_i$ , an integral quantity, hence not requiring an accurate radial resolution of the potential. Obtaining the correct angular current distribution typically requires  $r_b/n_r \lesssim 0.1$ . Second the chosen example is at moderate magnetization; when  $\beta_i \gtrsim 2$  the presheath tends to elongate along the magnetic axis, hence accurate angular resolution is essential. Usually  $n_\theta = n_\psi = 30$  proves satisfactory.

For production runs, we therefore set  $n_\theta = n_\psi = 30$  and  $n_r \simeq 10r_b$ , the domain radius  $r_b$  being chosen according to the plasma drift velocity to oversatisfy Eq. (9). The minimal number of

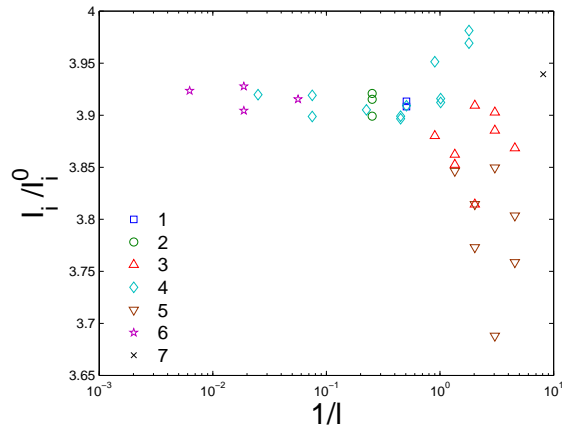


Figure 3: Ion saturation current as a function of  $1/l$ . Each point corresponds to a different SCEPTIC3D run, where  $l$  is varied by changing the number of operating processors  $n_{\text{proc}}$  (400k particles per processor) and the grid. (1 $\square$ ):  $n_{\text{proc}} = 512$ ,  $r_b = 8$ ,  $n_r = 120$ ,  $n_{\theta,\psi} = 30$ . (2 $\circ$ ):  $n_{\text{proc}} = 512$ ,  $r_b = 8$ ,  $n_r = 120$ ,  $n_{\theta,\psi} \leq 30$ . (3 $\triangle$ ):  $n_{\text{proc}} = 128$ ,  $r_b = 8$ ,  $n_r \geq 80$ ,  $n_{\theta,\psi} \geq 30$ . (4 $\diamond$ ):  $n_{\text{proc}} = 128$ ,  $r_b = 8$ ,  $n_r \geq 80$ ,  $n_{\theta,\psi} \leq 30$ . (5 $\nabla$ ):  $n_{\text{proc}} = 128$ ,  $r_b = 12$ ,  $n_r \geq 80$ ,  $n_{\theta,\psi} \geq 30$ . (6 $\star$ ):  $n_{\text{proc}} = 128$ ,  $r_b = 8$ ,  $n_r = 40$ ,  $n_{\theta,\psi} \leq 15$ . (7 $\times$ ):  $n_{\text{proc}} = 32$ ,  $r_b = 8$ ,  $n_r = 80$ ,  $n_{\theta,\psi} = 30$ .

particles such that noise levels be of no concern is then  $n_{\text{part}} \sim n_{\theta} n_{\psi} n_r^2 r_b$  at  $\tau = 0.1$  ( $l \sim 1$ ), and we allow without further optimization  $n_{\text{part}} \sim 0.5 n_{\theta} n_{\psi} n_r^2 r_b$  at higher ion temperature.

## 2.5 Axisymmetry resolution

SCEPTIC3D has the particularity of being built on a non isotropic grid with uniform  $\cos \theta$  spacing. This choice was motivated by the convenience to have, at a given radial position, a computational cell volume independent of  $\theta$ . The drawback of course is that extrapolating the particle positions to the grid, as well as interpolating the potential gradient back to the particles, requires special care to ensure second order accuracy. In fact only first order accuracy is reached on axis because when  $n_{\theta}$  is doubled,  $\Delta\theta$  is only divided by  $\sqrt{2}$ .

A stringent test of the grid implementation consists in checking that an axisymmetric case yields the same solution regardless of the physical axis orientation. Fig. (4) shows the average ion saturation flux-density  $\Gamma_i$ , as well as the average sheath entrance potential  $\phi_s$ , for the case  $\tau = 0.1$ ,  $v_d = c_{s0}$ ,  $\beta_i = 0$ . The solution is plotted as a function of the position projected on the drift axis ( $\cos \chi$ ), which is here the physical symmetry axis. It can be seen that the solutions at different drift angles are almost indistinguishable, except perhaps around  $\cos \chi \gtrsim 0.7$  on the  $\phi_s$  plot, which gives us strong confidence that the code performs properly.

Fig. (4a) also shows the ion flux calculated by the two-dimensional code SCEPTIC(2D), from the appendix in Ref. [15]. The excellent agreement between the 2D and 3D calculations, despite drastic evolutions between the two code versions, is a further benchmark of SCEPTIC3D. More important, it suggests that there is no spontaneous breaking of symmetry in axisymmetric cases, which could jeopardize the validity of prior 2D treatments.

The example shown here has been selected as one of the most computationally challenging, due

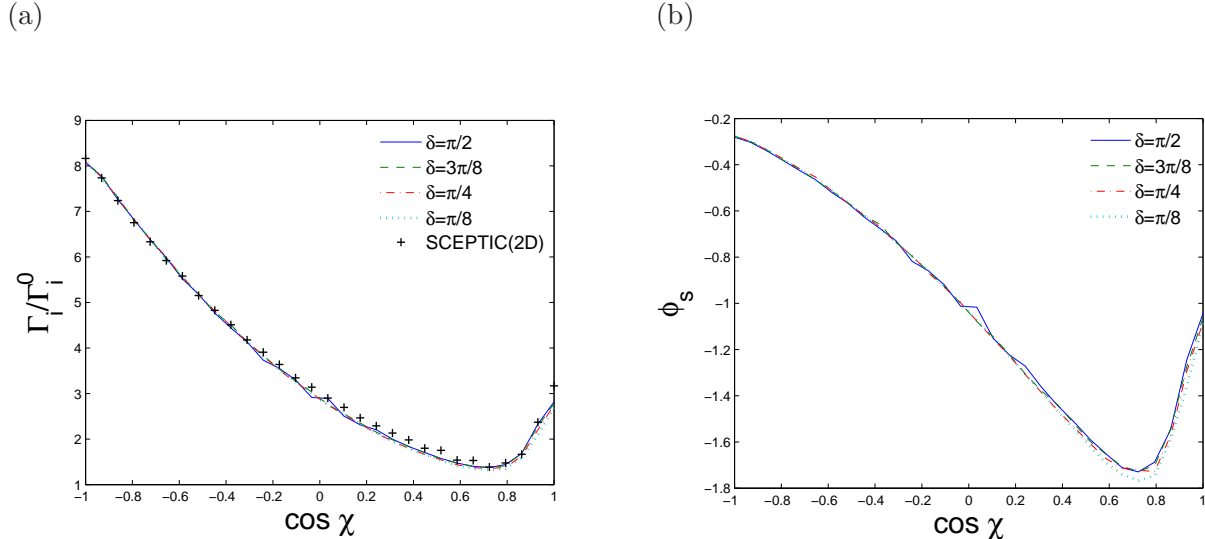


Figure 4: (a) Average ion saturation flux and (b) average sheath entrance potential as a function of the position projected on the drift axis ( $\cos \chi$ ), for the case  $\tau = 0.1$ ,  $v_d = c_{s0}$ ,  $\beta_i = 0$  and a selection of  $\delta$ . The points labeled “SCEPTIC(2D)” correspond to the solution from the appendix in Ref. [15]. SCEPTIC3D runs have been performed with  $r_b = 8$ ,  $n_r = 120$ ,  $n_\theta = n_\psi = 30$ , and  $n_{\text{part}} = 51.2M$ .

to the collection “bump” in the downstream region arising from ion focussing. More details on this feature will be given in paragraph 4.2.

### 3 Plasma profiles

#### 3.1 Infinite ion magnetization

##### 3.1.1 Density

Because flow and magnetic field are not aligned, plasma profiles are inherently three-dimensional unless  $\beta_i$  is large enough for the flow to be constrained in planes perpendicular to the convective electric field, as illustrated in Fig. (1).

Fig. (5) shows a selection of density contour plots computed by SCEPTIC3D in the plane  $\{0, \mathbf{e}_y, \mathbf{e}_z\}$  for  $\beta_i = 20$ , in other words an average ion Larmor radius equal to a twentieth of probe radius. In each case the upstream region is clearly unperturbed, and the fluid stream lines indicate that the collection flow tube originates from the unperturbed region. Of course kinetic effects cause individual ions to move across the stream lines, but intuitively the computational domain is large enough for the saturation current to be accurately computed. The simulation with  $\delta = \pi/2$  shown in Fig. (5b) allows easy comparison with the magnetic-free case, which has rotational symmetry around the drift axis. Because magnetized ion motion is constrained along the field lines, the downstream depleted region can only be replenished one-dimensionally and therefore extends much further than in the magnetic-free regime.

The density contours can directly be compared with independent one-dimensional calculations [13, 14], valid in the probe magnetic shadow defined by  $x^2 + y^2 \leq 1$  when  $\beta_i \gg 1$ . Those



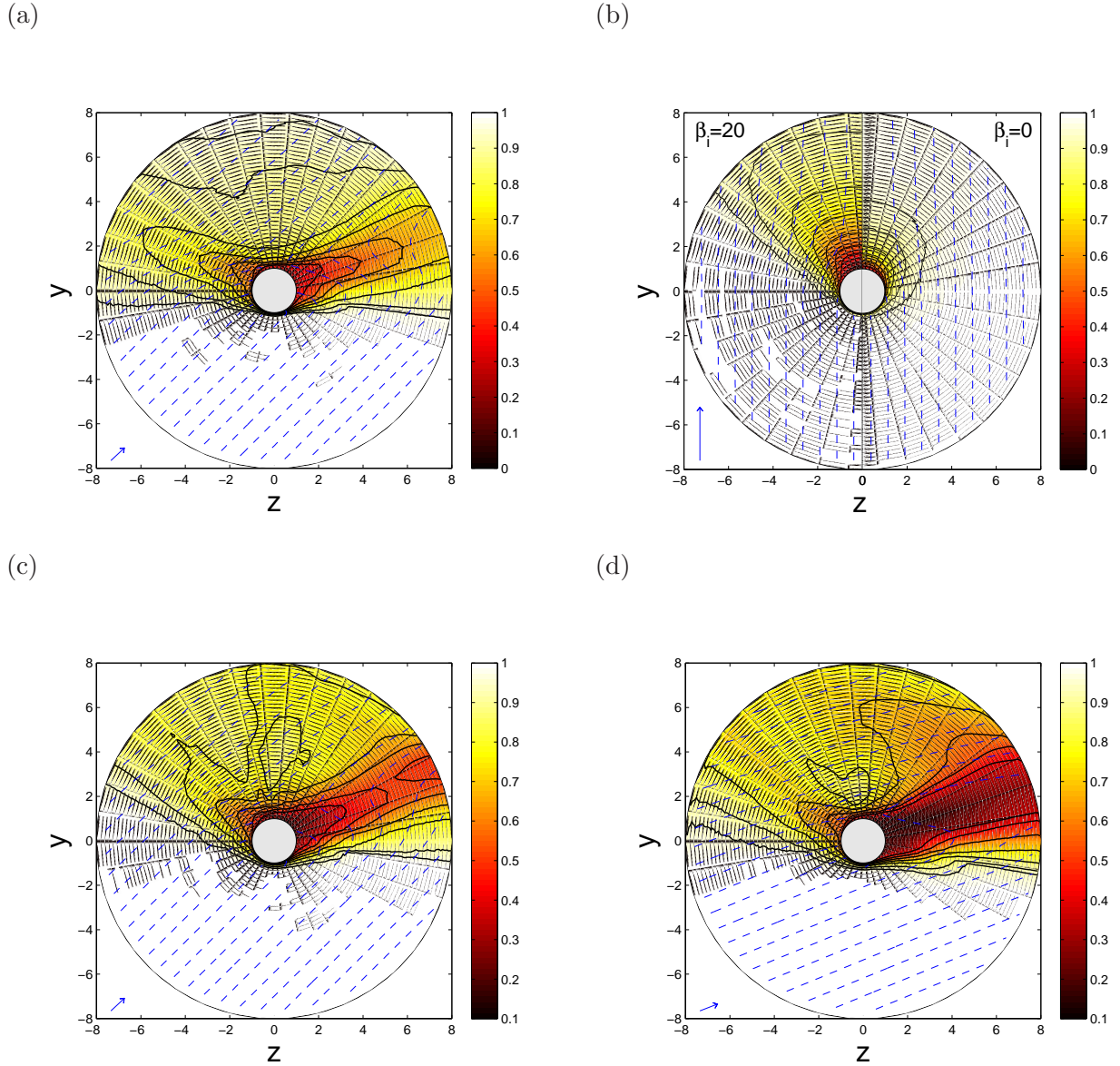


Figure 5: Selection of charge density contour plots in the plane  $\{0, \mathbf{e}_y, \mathbf{e}_z\}$ , with strongly magnetized ions  $\beta_i = 20$  (except in (b) where a comparison with the magnetic-free regime is provided). (a)  $\tau = 1$ ,  $v_d = 0.5c_{s0}$ ,  $\delta = \pi/4$ , (b)  $\tau = 1$ ,  $v_d = 1.5c_{s0}$ ,  $\delta = \pi/2$ , (c)  $\tau = 0.1$ ,  $v_d = 0.5c_{s0}$ ,  $\delta = \pi/4$  and (d)  $\tau = 0.1$ ,  $v_d = 0.5c_{s0}$ ,  $\delta = \pi/8$ . Iso-density contours for  $n = 0.4, 0.5, 0.6, 0.7, 0.8, 0.9, 0.95$  are full black, while fluid stream lines are dashed blue. The external velocity is indicated by a blue arrow on the figures' lower left corners.

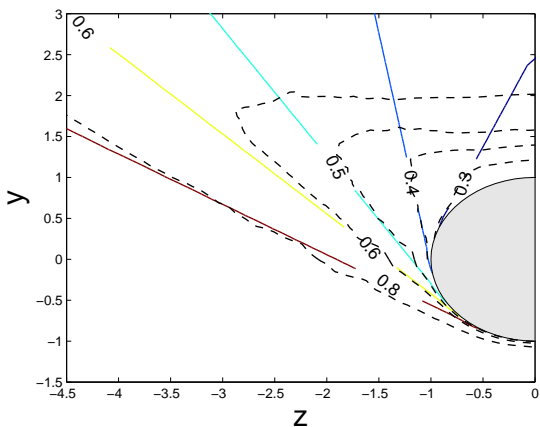
treatments show that the plasma density only depends on the angle  $\eta$ , defined in Fig. (1) as the angle between magnetic field and probe tangent in the plane of field and drift.

When  $\tau \lesssim 0.1$ , the isothermal fluid treatment of Ref. [13] according to which

$$n = \min \{1, \exp[-1 - (M_\infty - M_\perp \cot \eta)]\} \quad (11)$$

rigorously applies. A semi-analytic kinetic treatment such as Ref. [14] is required when the ion temperature is higher, although Eq. (11) remains a good approximation; recall that Mach numbers are normalized to  $c_{sI}$  (Eq. (5)). Fig. (6) compares SCEPTIC3D profiles with those one-dimensional calculations when  $\beta_i = 20$  and  $\delta = \pi/2$ , for (a)  $\tau = 0.1$ ,  $v_d = 0.5c_{s0}$  and (b)  $\tau = 1$ ,  $v_d = c_{s0}$ . It can be seen that the profiles agree extremely well (Less than 1% error on the isodensity lines angles), thus providing a successful second benchmark of SCEPTIC3D. Contour lines close behind the probe, but this effect is not captured by Refs [13, 14].

(a)



(b)

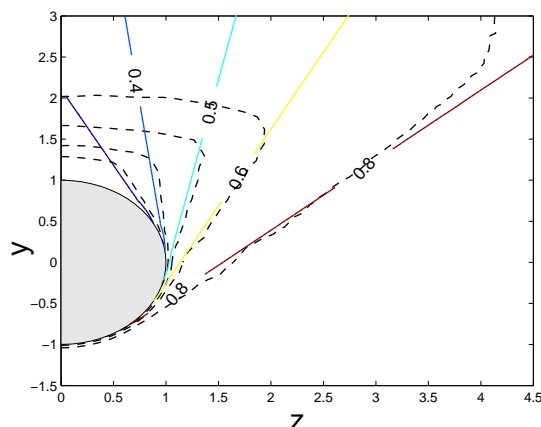


Figure 6: Comparison of density contour lines computed by SCEPTIC3D in the  $\{0, \mathbf{e}_y, \mathbf{e}_z\}$  plane (dashed black) with independent one-dimensional calculations (solid coloured) valid in the probe magnetic shadow when  $\beta_i \gg 1$ . Contours are for  $n = 0.8, 0.6, 0.5, 0.4, 0.3$ . SCEPTIC3D runs are performed with  $\beta_i = 20$ ,  $\delta = \pi/2$ , and (a)  $\tau = 0.1$ ,  $v_d = 0.5c_{s0}$  and (b)  $\tau = 1$ ,  $v_d = c_{s0}$ . One-dimensional calculations refer to (a) the isothermal formulation [13] and (b) the kinetic formulation [14].

Careful examination of Fig. (6) shows that there is a residual region on the probe leading edge where the one-dimensional calculations [13, 14] overestimate the density. This is due to an essential difference between the two approaches. SCEPTIC3D assumes the Debye sheath to be infinitesimally thin, but fully resolves the magnetic presheath where the ion Larmor motion is broken. Refs [13, 14] on the contrary assume the magnetic presheath to be infinitesimal as well, hence the density difference between SCEPTIC3D and those analytic theories is effectively the change across the magnetic presheath.

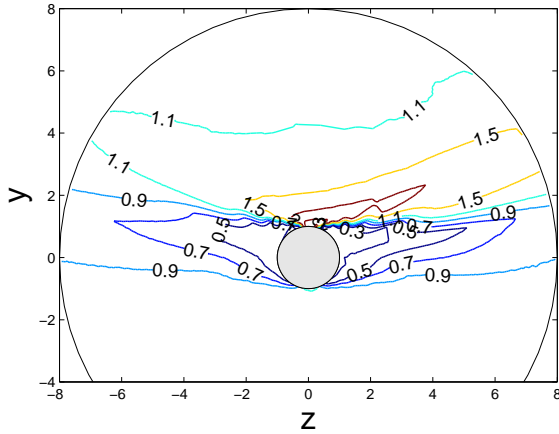
### 3.1.2 Ion temperature

SCEPTIC3D calculates the ion temperature symmetric tensor  $\bar{\bar{T}}_i$  in spherical coordinates, which upon rotation yields the Cartesian components  $T_{i,ab} = m (\langle v_a v_b \rangle - \langle v_a \rangle \langle v_b \rangle)$ . The magnetic moment of gyrating particles is an adiabatic invariant in the strong magnetization limit, at least outside the magnetic presheath. In the bulk plasma therefore,  $\bar{\bar{T}}_i$  expressed in the coordinates  $(x, y, z)$  is diagonal, and only  $T_{i,zz}$  can depart from the external temperature  $T_{i\infty}$ .

Fig. (7) shows contour plots of  $T_{i,zz}$  normalized to  $T_{i\infty}$  for the physical parameters of Fig. (5a,b), in the plane  $\{0, \mathbf{e}_y, \mathbf{e}_z\}$ .  $T_{i,zz}$  drops in the magnetic shadow as the ions are accelerated along the field, with straight isolines tangent to the probe surface [14]. The temperature drop exactly follows the law  $T_{i,zz}/T_{i\infty} = (N/N_\infty)^2$  in the limit  $\tau \ll 1$ , and approximately otherwise [14]. In other words, the temperature perturbation extends along the magnetic shadow much further than the density perturbation, as can be seen in Fig. (7a) where the tube  $T_{i,zz} \leq 0.9T_{i\infty}$  is almost parallel to the magnetic axis.

$T_{i,zz}$  sharply increases where the two counterstreaming ion populations present in the right and left magnetic shadows merge (in theory  $T_{i,zz} \rightarrow \infty$  at  $y = 1^+$  and  $z = 0$ ). Because our simulation is collisionless, the ion distribution function can decay back to the drifting Maxwellian only by convection, hence  $T_{i,zz}$  contours at  $y > 1$  are wing-shaped. Fig. (7b) shows, as first noticed in Fig. (5b), that the perturbation is much more localized in the absence of magnetic field.

(a)



(b)

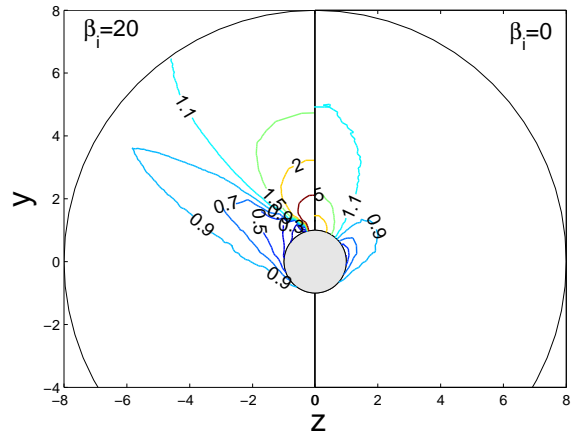


Figure 7: Contour plots of  $T_{i,zz}/T_{i\infty}$  in the plane  $\{0, \mathbf{e}_y, \mathbf{e}_z\}$ , with strongly magnetized ions  $\beta_i = 20$  (except in (b) where a comparison with the magnetic-free regime is provided). (a)  $\tau = 1$ ,  $v_d = 0.5c_{s0}$ ,  $\delta = \pi/4$  and (b)  $\tau = 1$ ,  $v_d = 1.5c_{s0}$ ,  $\delta = \pi/2$ .

### 3.2 Intermediate ion magnetization

In our quasineutral treatment, radial density gradients in the infinitesimal Debye sheath are infinite on the presheath length scale. Therefore regardless of the ion magnetization, density contour surfaces are tangent to the sheath entrance. Those surfaces need however not be straight lines in

$\{\mathbf{e}_y, \mathbf{e}_z\}$  cross-sections, and show in fact a fully three-dimensional structure.

Fig. (8) shows charge density contour plots in (a) the  $\{0, \mathbf{e}_y, \mathbf{e}_z\}$  and (b) the  $\{0, \mathbf{e}_x, \mathbf{e}_y\}$  planes for a run with intermediate ion magnetization  $\beta_i = 0.5$ . Fig. (8a) is qualitatively different from, say, Fig. (5c), because the magnetic presheath is thicker hence the upstream density does not seem to sharply drop at the probe surface. More interesting is Fig. (8b), reporting a significant anisotropy of density and fluid streamlines in the major cross-field cross-section  $\{0, \mathbf{e}_x, \mathbf{e}_y\}$  arising from two combined finite Larmor radius effects.

The first effect is the so-called magnetic presheath displacement, most noticeable where the probe surface is parallel to the convective electric field. For our sphere the corresponding region is  $x \sim 0$ , but for an infinite cylinder (regardless of the cross-section shape) whose axis is parallel to  $\mathbf{E}_{\text{conv}}$  the entire probe would be affected. The magnetic presheath displacement corresponds to the ion flow being diverted in the direction of the convective electric field by an “ $\mathbf{E} \wedge \mathbf{B}$ ” drift arising from the radial sheath-edge potential gradient. A schematic view of the phenomenon is proposed in Fig. (7) from Ref. [20], for a semi-infinite cylindrical probe with quadrilateral cross-section (note that the axis are oriented differently in Ref. [20]:  $\mathbf{E}_{\text{conv}} \parallel \mathbf{e}_z$  and  $\mathbf{B} \parallel \mathbf{e}_x$ ).

The second effect is strongest where the probe surface is normal to the convective electric field, corresponding for our sphere to  $x \sim \pm 1$ . At  $y \sim 0$  and positive  $x$ , the probe induced field adds to  $\mathbf{E}_{\text{conv}}$  and increases the “ $\mathbf{E} \wedge \mathbf{B}$ ” drift in the  $\mathbf{e}_y$  direction, while at negative  $x$  the fields tend to cancel out, reducing  $\mathbf{v}_y$ . This  $\mathbf{v}_y$  modulation in turns affects the relative weight of the probe-induced polarization drift, creating an anisotropy in ion collection (Increased collection at  $x < 0$  and decreased collection at  $x > 0$ ).

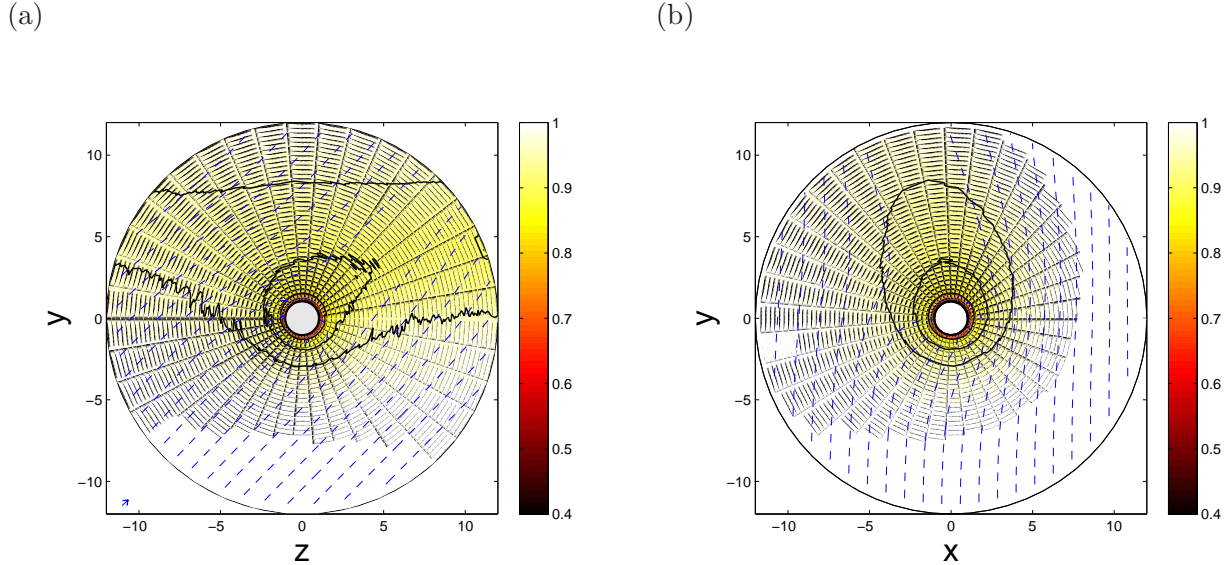


Figure 8: Charge density contour plots in the (a)  $\{0, \mathbf{e}_y, \mathbf{e}_z\}$  plane and (b)  $\{0, \mathbf{e}_x, \mathbf{e}_y\}$  plane, with plasma parameters  $\tau = 0.1$ ,  $v_d = 0.2c_{s0}$ ,  $\delta = \pi/4$ ,  $\beta_i = 0.5$ . The asymmetry in (b) is due to finite Larmor radius effects. Iso-density contours are full black, while fluid stream lines are dashed blue.

## 4 Ion saturation current

### 4.1 Free-flight current

While numerically computed plasma profiles are an important tool to understand the physics of plasma-object interaction, the most useful quantity to be compared with experimental measurements is the total ion saturation current, and possibly its angular distribution. We start the discussion in the free-flight regime, corresponding to the neglect of probe-induced electric fields on the ions while still accounting for  $\mathbf{E}_{\text{conv}}$ . This treatment is appropriate in the limit  $\tau \gg 1$ , because the electron pressure is then strongly outweighed by the ion pressure.

When the ions are strongly magnetized, the total saturation current can be obtained by summing the flux density to “slices” in the plane of flow and magnetic field such as shown in Fig. (1a):

$$I_i^{|\beta_i=\infty} = R_p^2 \int_{-1}^1 \int_0^{2\pi} \Gamma_{i\parallel}^{|\beta_i=\infty}(\eta) (1-x^2)^{1/2} |\sin \eta| d\eta dx = \frac{\pi}{2} R_p^2 \int_0^{2\pi} \Gamma_{i\parallel}^{|\beta_i=\infty}(\eta) d\eta, \quad (12)$$

where  $R_p (1-x^2)^{1/2}$  is the cross-section radius at position  $x$  along  $\mathbf{e}_x$ .  $I_i^{|\beta_i=\infty}$  can then be calculated, although not in closed form, with the free-flight strongly magnetized ion flux distribution [14]

$$\Gamma_{i\parallel}^{|\beta_i=\infty}(\eta) = \Gamma_i^0 \left\{ \exp(-\mu_{ti}^2) + \sqrt{\pi} \mu_{ti} [\pm 1 + \text{erf}(\mu_{ti})] \right\}, \quad (13)$$

where

$$\mu_{ti} = \frac{v_{\perp} \cot \eta - v_{\infty}}{v_{ti}}, \quad (14)$$

and “ $\pm$ ” stands for “+” downstream, and “-” upstream. To first order in  $1/\beta_i$ , the effect of finite ion magnetization on the total ion current can be accounted for by changing  $R_p^2$  to  $R_p^2(1 + 2/\beta_i)$  in Eq. (12). Such substitution is equivalent to saying that to first order in  $1/\beta_i$ , the ions see a probe with effective radius  $R_p + R_L$ ; recall that  $\beta_i = R_p/R_L$ , where  $R_L$  is the *average* ion Larmor radius. The ion current is then

$$I_i(\beta_i) = I_i^{|\beta_i=\infty} \left( 1 + \frac{2}{\beta_i} \right) + O\left(\frac{1}{\beta_i}\right)^2. \quad (15)$$

In the particular case  $\delta = 0$ , or  $v_{\perp} = 0$ , the problem is rotationally symmetric around the probe magnetic axis, and semi-analytic calculations can be performed (See Ref. [16] for an overview, and Ref. [21] for detailed calculations). To first order in  $\beta_i$ :

$$I_i(\beta_i) = I_i^0 \left\{ \left[ \frac{1}{2} \exp(-\mu_{ti}^2) + \frac{\sqrt{\pi}}{2} \left( \mu_{ti} + \frac{1}{2\mu_{ti}} \right) \text{erf}(\mu_{ti}) \right] - \exp(-\mu_{ti}^2) \frac{\beta_i}{3\pi} \right\} + O(\beta_i)^2, \quad (16)$$

with  $\mu_{ti} = -v_{\infty}/v_{ti}$ .

Fig. (9) shows the free-flight current dependence on  $\beta_i$  for different drift angles  $\delta$ , when (a)  $v_d = 0.25v_{ti}$  and (b)  $v_d = v_{ti}$ . It can be seen that  $I_i$  is a decreasing function of  $\beta_i$  regardless of  $\delta$ , and an increasing function of  $\delta$  (for  $\delta \in [0 : \pi/2]$ ) regardless of  $\beta_i$ . The solution exactly matches the independent semi-analytic calculation of Refs [16, 21] at  $\delta = 0$ , as well as the expansion (15) at large  $\beta_i$ , which is a good benchmark of the magnetized particle mover implementation in SCEPTIC3D.

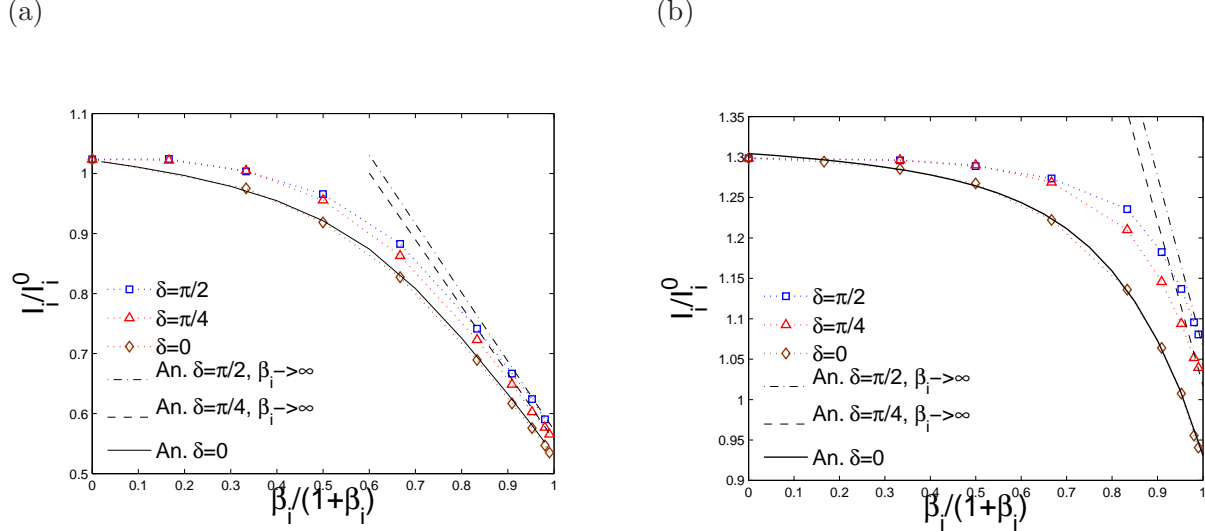


Figure 9: Total ion saturation current normalized to  $I_i^0 = 4\pi R_p^2 v_{ti}/2\sqrt{\pi}$  as a function of ion magnetization  $\beta_i$  in the free-flight regime (i.e. disregarding probe-induced electric field effects on the ions), computed by SCEPTIC3D for different angles of flow and magnetic field  $\delta$ . “An.  $\delta = 0$ ” refers to the semi-analytic treatment of Refs [16, 21] for which the weak field limit is given by Eq. (16). “An.  $\beta_i \rightarrow \infty$ ” refers to the high field expansion (15). (a)  $v_d = 0.25v_{ti}$  and (b)  $v_d = v_{ti}$ .

## 4.2 Self-consistent ion current

When the ion temperature is finite and the self-consistent potential distribution around the probe needs to be accounted for, Eq. (12) should be used with  $\Gamma_{i\parallel}^{|\beta_i=\infty}$  from the semi-analytic kinetic solution of Ref. [14]. The high field expansion (15) is then incorrect, but we can argue, at least heuristically by physical continuity, that  $I_i(\beta_i)$  still has a  $1/\beta_i$  term at high  $\beta_i$ . This property is essential because it allows us to connect the current computed by SCEPTIC3D at reasonably high  $\beta_i$ , typically  $\beta_i \lesssim 50$ , to Eq. (12) at  $\beta_i = \infty$ .

Fig. (10) shows the ion saturation current as a function of  $\beta_i$  for different plasma conditions. (a)  $\tau = 0.1$ ,  $v_d = 0.25c_{s0}$ , (b)  $\tau = 1$ ,  $v_d = 0.5c_{s0}$  and (d)  $\tau = 1$ ,  $v_d = 1.5c_{s0}$  are qualitatively similar, although the latter corresponds to a supersonic flow. The current slope at  $\beta_i = 0$  seems to be zero, but there is always a linear term be it smaller than what the code can resolve. The dashed portions of curves at high  $\beta_i$  connect the last point from SCEPTIC3D calculations to  $I_i^{|\beta_i=\infty}$  (Eq. (12) with  $\Gamma_{i\parallel}^{|\beta_i=\infty}$  from Ref. [14]); because there is no slope discontinuity at the connection, we can *a posteriori* confirm that the ion current has indeed a  $1/\beta_i$  dependence at high  $\beta_i$ .

When the ion temperature is small and the drift velocity approximately sonic, the ion current has the unexpected property of peaking at intermediate magnetization. An example of such behaviour is shown in Fig. (10c), for the case  $\tau = 0.1$  and  $v_d = c_{s0}$ . The peak is maximum for  $\delta = \pi/2$ , and decreases with  $\delta$ . We have not run self-consistent cases with  $\delta = 0$ , as a rigorous treatment would involve modeling anomalous cross-field transport in the elongated presheath [23, 24]. However approximate collisionless solutions for  $\beta_i \leq 1$  [16] suggest that the current does not peak when the flow is field aligned.

Fig. (11) shows the ion flux-density to the probe major cross-section in the plane of flow and

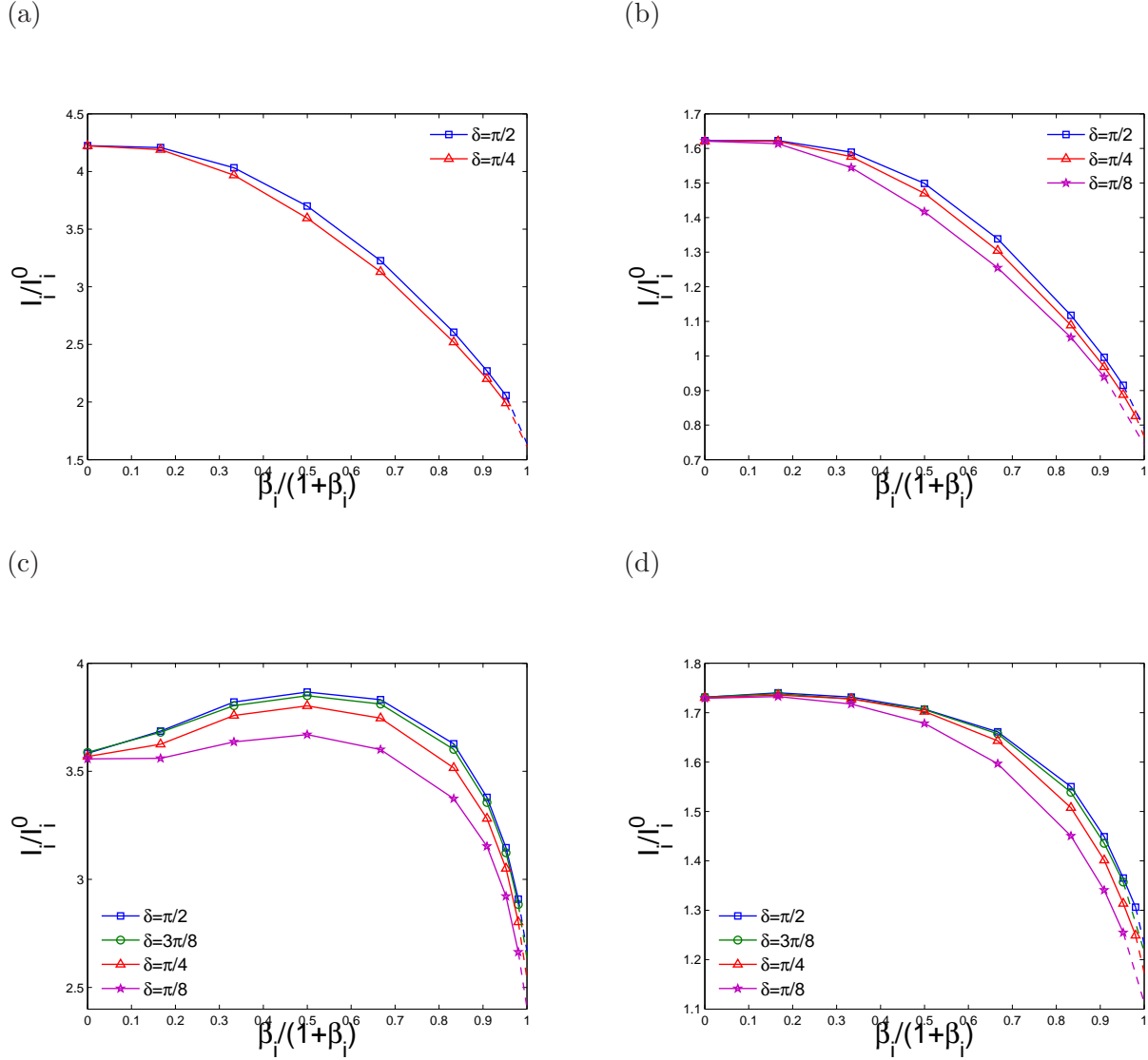


Figure 10: Total ion saturation current normalized to  $I_i^0 = 4\pi R_p^2 v_{ti} / 2\sqrt{\pi}$  as a function of ion magnetization  $\beta_i$ , self-consistently calculated with SCEPTIC3D. (a)  $\tau = 0.1$ ,  $v_d = 0.25c_{s0}$ . (b)  $\tau = 1$ ,  $v_d = 0.5c_{s0}$ . (c)  $\tau = 0.1$ ,  $v_d = c_{s0}$ . (d)  $\tau = 1$ ,  $v_d = 1.5c_{s0}$ . The dashed portions of curves at high  $\beta_i$  connect our simulations at finite magnetization to  $I_i^0$  ( $\beta_i \rightarrow \infty$ ) (Eq. (12) with  $\Gamma_{i\parallel}^{\beta_i \rightarrow \infty}$  from Ref. [14]).

magnetic field  $\{0, \mathbf{e}_y, \mathbf{e}_z\}$ , as a function of  $\cos \theta$ ; the curves are therefore closed on themselves, the upper portions corresponding to  $\sin \theta \leq 0$  and the lower portions to  $\sin \theta \geq 0$ . As expected, both solutions (a)  $\tau = 1$ ,  $v_d = c_{s0}$ ,  $\delta = \pi/4$  and (b)  $\tau = 0.1$ ,  $v_d = c_{s0}$ ,  $\delta = 3\pi/8$  tend to the prediction of Ref. [14] when  $\beta_i \rightarrow \infty$ . If it were plotted as a function of  $\cos(\theta - \delta)$ , the curve  $\beta_i = 0$  in Fig. (11b) would perfectly match the curves in Fig. (4a). Both figures indeed correspond to the same plasma conditions, and  $\chi = \theta - \delta$  on the probe major cross-section. The difference is that Fig. (4a) has been created with current data from the entire probe surface, while Fig. (11b) with current data from the probe major cross-section only.

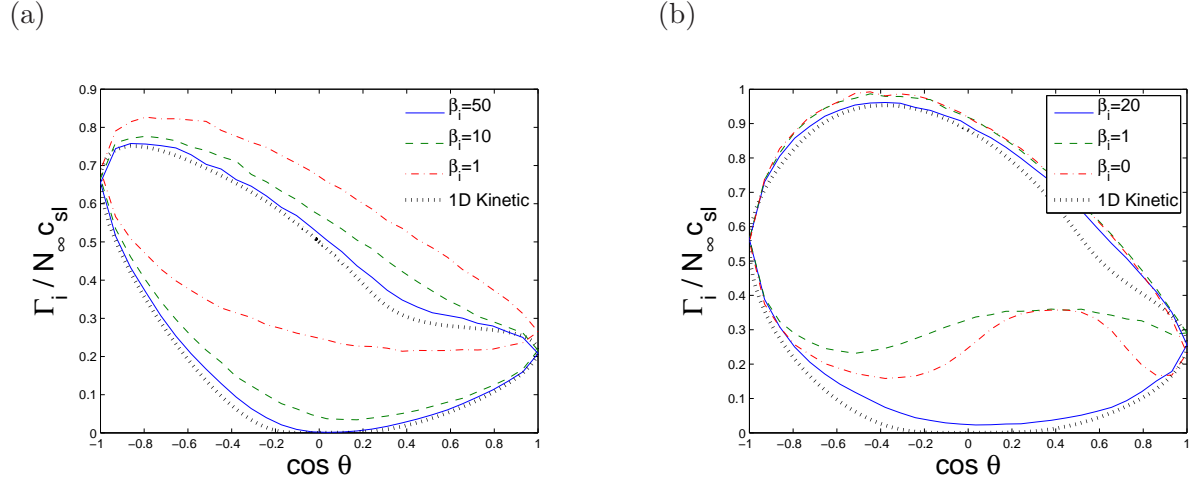


Figure 11: Angular ion flux-density distribution to the probe major cross-section in the plane of flow and magnetic field  $\{0, \mathbf{e}_y, \mathbf{e}_z\}$  normalized to  $N_\infty c_{sI}$ , self-consistently calculated with SCEPTIC3D for different ion magnetizations  $\beta_i$ . “1D Kinetic” refers to the semi-analytic solution of Ref. [14]. (a)  $\tau = 1$ ,  $v_d = c_{s0}$  and  $\delta = \pi/4$ . (b)  $\tau = 0.1$ ,  $v_d = c_{s0}$  and  $\delta = 3\pi/8$ .

Fig. (11b) also helps understand the ion saturation current peak at  $\beta_i \sim 1$ . When  $\beta_i = 0$ , the probe focusses the ions downstream, creating the “bump” first seen in Fig. (4a). As  $\beta_i$  increases, part of the ions that would miss the probe in the absence of magnetic field are collected downstream while the upstream current is unaffected. Eventually when  $\beta_i$  increases further, the dynamics becomes one-dimensional and focussing is suppressed.

### 4.3 Transverse Mach probe calibration

Transverse Mach probes seek to measure the external plasma drift velocity by comparing the ion saturation flux-density  $\Gamma_i$  at different angles in a given plane of flow and magnetic field. The two main competing designs are rotating planar probes, and Gundestrup probes, operating simultaneous measurements at different angles with a set of electrodes spanning a single probe head [22]. It is here convenient to think in terms of  $M_\infty$  and  $M_\perp$  rather than  $v_d$  and  $\delta$ .

It was argued in Ref. [14] that the only transverse spherical Mach probe calibration method valid at moderate drift for infinite and negligible ion magnetization, yet involving a single calibration factor  $M_c$ , consists in measuring the two flux ratios  $R_{3\pi/4} = \Gamma_i(\eta = -\pi/4)/\Gamma_i(\eta = 3\pi/4)$  and



$R_{\pi/4} = \Gamma_i(\eta = -3\pi/4)/\Gamma_i(\eta = \pi/4)$ , and relating them to the external flow by

$$M_{\perp} = \frac{M_c}{2} (\ln R_{3\pi/4} - \ln R_{\pi/4}) \quad (17)$$

$$M_{\infty} = \frac{M_c}{2} (\ln R_{3\pi/4} + \ln R_{\pi/4}). \quad (18)$$

Measures can in theory be made in any plane of flow and magnetic field, although it is best to avoid grazing planes located at  $x \sim \pm 1$ . Fig. (12) shows a three-dimensional view of the probe surface, color-plotted according to the local ion flux density for the example  $\tau = 0.3$ ,  $v_d = 0.5c_{s0}$ ,  $\delta = \pi/4$  and  $\beta_i = 2$ . The most obvious possible plane of measurement is indicated by a dotted circle corresponding to the major cross-section ( $x = 0$ ), best mocking an infinite cylindrical probe. Two more options are a solid and dashed circles, corresponding to quarter cross-sections at  $x = \pm 1/\sqrt{3}$ , whose particularity is to cut the sphere at points with  $x = \pm y = \pm z$  exactly where Mach probe measurements are to be made (i.e.  $\tan \eta = \pm 1$ ). Those configurations therefore best mock the pyramidal probe of Smick and Labombard [9], where measures are taken on planar electrodes at  $45^\circ$  angle with the three coordinate planes.

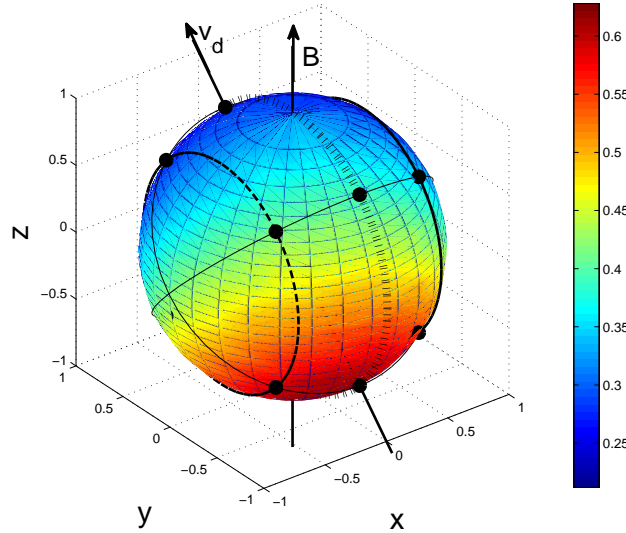


Figure 12: Three dimensional view of the probe surface, color-plotted according to the normalized ion saturation flux  $\Gamma_i/(N_{\infty}c_{sI})$  for the plasma parameters  $\tau = 0.3$ ,  $v_d = 0.5c_{s0}$ ,  $\delta = \pi/4$  and  $\beta_i = 2$ . The dotted, solid and dashed circles respectively correspond to cross sections located at  $x = 0, 1/\sqrt{3}, -1/\sqrt{3}$ , and the thick dots to the points where Mach probe measurements are to be made (i.e.  $\tan \eta = \pm 1$ ).

In the limit  $\beta_i = \infty$ ,  $M_c$  does not depend on the measurement cross-section and is given by [14]

$$M_c^{|\beta_i=\infty} = \frac{1}{2}\kappa + \frac{1}{\sqrt{2\pi}}(1 - \kappa), \quad \text{with} \quad \kappa(\tau) \simeq \frac{1}{2}\text{erfc}(0.12 + 0.40 \ln \tau). \quad (19)$$

In the opposite limit  $\beta_i = 0$ , early simulations with SCEPTIC [15] have shown that the ion saturation flux distribution to a spherical probe is approximately given by  $\Gamma_i \propto \exp(-K(\cos \chi)v_d/2)$ ,

where again  $\cos \chi$  is the position projected on the drift axis, and  $K \simeq 1.34/c_{s0}$  for  $\tau \lesssim 3$ . The flux ratio at angle  $\eta + \pi$  over  $\eta$  is therefore  $R = \exp(K|\cos(\chi)|v_d)$ , yielding for measurements with  $\tan \eta = \pm 1$  at poloidal position  $\psi$ :

$$M_c^{|\beta_i=0} = \frac{2}{Kc_{sI}} \frac{|\sin \psi|}{\sqrt{1 + (\sin \psi)^2}}. \quad (20)$$

On the *major* cross-section,  $|\sin \psi| = 1$ , hence  $M_c^{|\beta_i=0} = \sqrt{2}/(Kc_{sI})$ . In particular at  $\tau = 1$  where  $K = 1.34/c_{s0}$ :  $M_c^{|\beta_i=0} \simeq 0.75$  (and  $M_c^{|\beta_i=\infty} \simeq 0.44$ ).  $\psi$  is not constant on the quarter cross-sections since on the sphere surface  $x = \sin \theta \cos \psi$ . However at the points where  $\tan \eta = \pm 1$ ,  $\tan \psi = \pm 1$  as well, therefore at  $\tau = 1$  on the *quarter* cross-sections:  $M_c^{|\beta_i=0} = 0.91$  (and still  $M_c^{|\beta_i=\infty} \simeq 0.44$ ).

At intermediate magnetization, there is no *a priori* reason to believe that Eqs. (17,18) still hold. Perhaps the most important result of this publication is that they actually do, to well within experimental uncertainty. This can easily be seen on Fig. (13), where  $R_{3\pi/4}$  and  $1/R_{\pi/4}$  on the major cross section  $\{0, \mathbf{e}_y, \mathbf{e}_z\}$  from SCEPTIC3D simulations are plotted in log-space against  $M_\perp + M_\infty$  and  $M_\perp - M_\infty$ , for the particular case  $\tau = 1$ . The points with  $v_d \lesssim c_{sI}$  can be fitted to a line with slope  $1/M_c$ , identical for  $R_{3\pi/4}$  and  $R_{-\pi/4}$ , and function of  $\beta_i$  only.

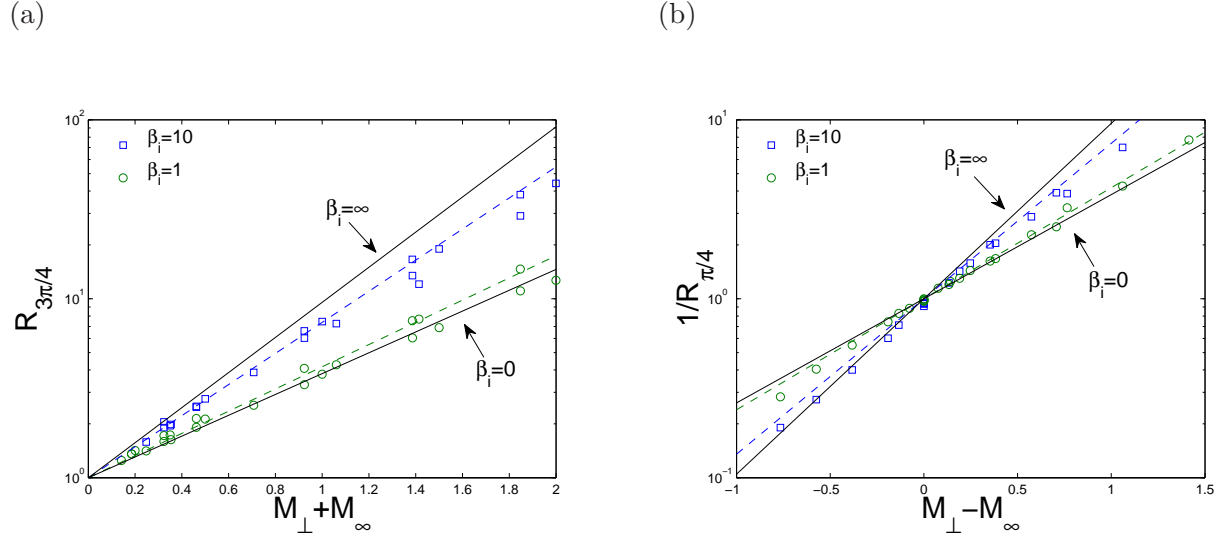


Figure 13: Upstream to downstream flux ratio on the probe major cross-section at (a)  $\eta = 3\pi/4$  and (b)  $\eta = \pi/4$ , versus respectively  $M_\perp + M_\infty$  and  $M_\perp - M_\infty$ , from a large set of SCEPTIC3D runs spanning  $v_d \in [0 : 1.5]c_{s0}$  and  $\delta \in [\pi/8 : \pi/2]$ . Also shown are the corresponding fitting lines, whose slopes  $1/M_c$  are taken from Fig. (14a).

The calibration factors  $M_c$  in the entire range of ion magnetization and for  $\tau \in [0.1 : 10]$ , computed by fitting SCEPTIC3D’s solutions with  $v_d \lesssim c_{sI}$  and  $\delta \in [\pi/8 : \pi/2]$ , are plotted in Fig. (14) on (a) on the major cross-section and (b) the quarter cross-sections. The fitting error bars, shown in Fig. (14a), are thinner at low and large  $\beta_i$ , where the error mostly arises from numerical noise, and thicker at  $\beta_i \simeq 0$  where part of the error is due to Eqs (17,18) being approximate. Because there never seems to be more than  $\sim 10\%$  uncertainty, Eqs (17,18) can be assumed to be “correct” for experimental purposes.

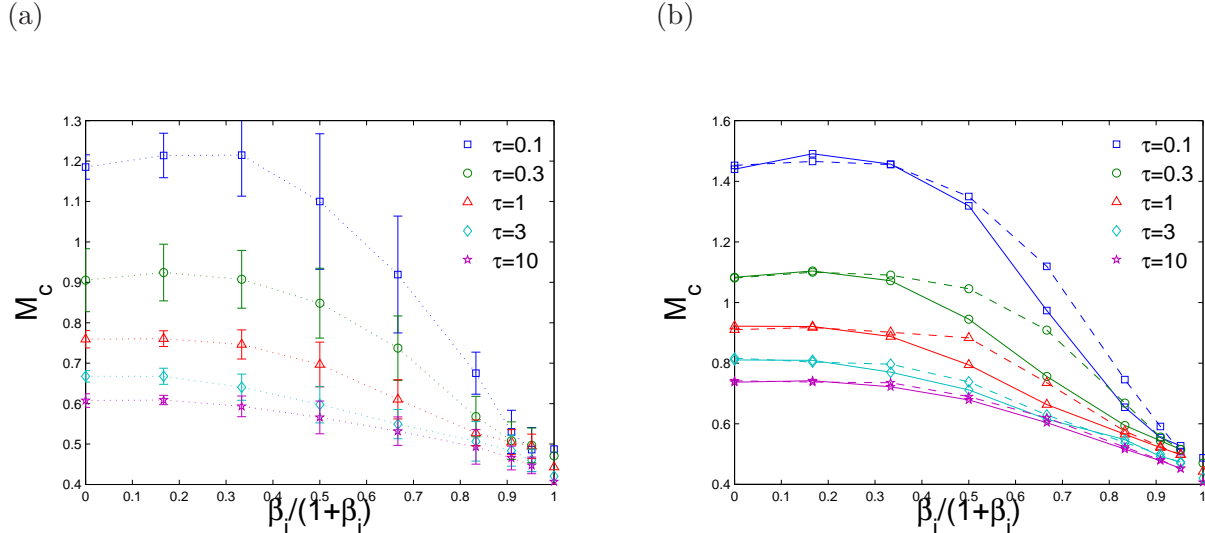


Figure 14: Transverse Mach probe calibration factor  $M_C$  as a function of magnetization  $\beta_i$  and temperature ratio  $\tau$  computed with SCEPTIC3D for measurements made (a) on the major cross-section and (b) the quarter cross-sections. (a) also shows the fitting error bars, arising from numerical noise and from Eqs (17,18) being only approximate. On (b), solid lines refer to measurements at  $x = 1/\sqrt{3}$ , and dashed lines to measurements at  $x = -1/\sqrt{3}$ . The points at  $\beta_i = \infty$  are given by Eq. (19).

Error bars have not been plotted on Fig. (14b) to increase readability, but are qualitatively similar to those in Fig. (14a). The noticeable result is here that at intermediate magnetization, Mach probes with electrodes whose normal is not on the plane of flow and magnetic field are sensible to the magnetic field orientation. This is a consequence of the finite Larmor radius effects observed in Fig. (8); in particular the flow deflection towards the region  $x \lesssim 0$  seen in Fig. (8b) causes the flux ratios to be lower at  $x = -1/\sqrt{3}$  than  $x = 1/\sqrt{3}$ .

## 5 Summary and conclusions

The hybrid Particle in cell code SCEPTIC3D has been specifically designed to solve the self-consistent interaction of a negatively biased sphere with a transversely flowing collisionless magnetoplasma. We report in this publication results in the regime of infinitesimal Debye length, when the plasma region of interest is quasineutral, for a wide range of temperatures and drift velocities.

In the limit of strong ion magnetization, the problem is two-dimensional and each plane of flow and magnetic field can be treated independently; the analytic or semi-analytic solutions [13, 14] yielding the magnetic shadow profiles and ion saturation flux then apply. At intermediate magnetization, when the ion Larmor radius compares to the probe radius, the plasma profiles show a complex three-dimensional structure. In particular we observe the effect of magnetic presheath displacement described in Ref. [20], as well as polarization drift modulation where the probe surface is grazing the magnetic field. An unexpected finding in this regime is that for cold ions and close to sonic flows, the total saturation current peaks here.

Although the full ion charge flux distribution to the probe depends on the plasma parameters

in a non-straightforward way, the major result of this study is that flux ratios at  $\pm 45^\circ$  to the magnetic field in planes of flow and magnetic field can very easily be related to the external Mach numbers. To within  $\sim 10\%$  accuracy (at least for  $\tau \geq 0.1$ ), there exists a single factor  $M_c$ , function of magnetization  $\beta_i$  and temperature ratio  $\tau$  only, such that  $M_\perp$  and  $M_\infty$  satisfy Eqs (17,18). Except at infinite magnetization,  $M_c$  is probe-shape dependent, and sphere solutions on the major and quarter cross-sections are given in Fig. (14). This provides the theoretical calibration for transverse Mach probes with appropriately placed electrodes. Of course probes are rarely spherical in practice, nevertheless we believe that the provided solutions should reasonably well apply to respectively infinite cylindrical probes with circular cross-section, and pyramidal probes such as the Alcator C-mod WASP [9].

## Acknowledgments

Leonardo Patachini was supported in part by NSF/DOE Grant No. DE-FG02-06ER54891. The authors are grateful to John C. Wright for helping them porting SCEPTIC3D on the MIT PSFC Parallel Opteron/Infiniband cluster Loki, where most calculations were performed.

## References

- [1] I.H. Hutchinson, *Principles of Plasma Diagnostics*, 2nd ed. (Cambridge University press, Cambridge, UK, 2002).
- [2] F. Wagner, G. Becker, D. Campbell *et al*, *Regime of Improved Confinement and High Beta in Neutral-Beam-Heated Divertor Discharges of the ASDEX Tokamak*, Phys. Rev. Letters **49** 1408 (1982).
- [3] K.H. Burrell, E.J. Doyle, P. Gohil *et al*, *Role of the radial electric field in the transition from L (low) mode to H (high) mode to VH (very high) mode in the DIII-D tokamak*, Phys. Plasmas **1**(5) 1536, (1994).
- [4] A.J.H. Donné, *Diagnostics for current density and radial electric field measurements: overview and recent trends*, Plasma Phys. Control. Fusion **44** B137 (2002).
- [5] B. LaBombard, J.W. Hughes, N. Smick *et al*, *Critical gradients and plasma flows in the edge plasma of Alcator C-mod*, Phys. Plasmas **15**(5) 056106 (2008).
- [6] C.S. MacLatchy, C. Boucher, D.A. Poirier *et al*, *Gundestrup: A Langmuir/Mach probe array for measuring flows in the scrape-off layer of TdeV*, Rev. Sci. Instrum. **63**(8) 3923 (1992).
- [7] P.M. Chung, L. Talbot and K.J. Touryan, *Electric Probes in Stationary and Flowing Plasmas: Theory and Application*, (New York:Springer, 1975).
- [8] G.F. Matthews, S.J. Fielding, G.M. McCracken *et al*, *Investigation of the fluxes to a surface at grazing angles of incidence in the tokamak boundary*, Plasma Phys. Control. Fusion **32**(14) 1301 (1990).
- [9] N. Smick and B. LaBombard, *Wall scanning probe for high-field side plasma measurements on Alcator C-mod*, Rev. Sci. Instrum. **80**(2) 023502 (2009).

- [10] V.E. Fortov, A.C. Ivlev, S.A. Khrapak *et al* *Complex (dusty) plasmas: Current status, open issues, perspectives*, Physics reports **421** 1-103 (2005).
- [11] Y.L. Alpert, A.V. Gurevich and L.P. Pitaevskii *Space Physics with Artificial Satellites*, Consultants Bureau (1965).
- [12] S.H. Brecht, J.G. Luhmann and D.J. Larson, *Simulation of the Saturnian magnetospheric interaction with Titan*, J. Geo. Research **105**(A6) 13119 (2000).
- [13] I.H. Hutchinson, *Ion Collection by Oblique Surfaces of an Object in a Transversely Flowing Strongly Magnetized Plasma*, Phys. Rev. Lett. **101** 035004 (2008).
- [14] L. Patacchini and I.H. Hutchinson, *Kinetic solution to the Mach probe problem in transversely flowing strongly magnetized plasmas*, (To be published).
- [15] I.H. Hutchinson, *Ion collection by a sphere in a flowing plasma: 1. Quasineutral*, Plasma Phys. Control. Fusion **44**, 1953-1977 (2002).
- [16] L. Patacchini and I.H. Hutchinson *Angular distribution of current to a sphere in a flowing, weakly magnetized plasma with negligible Debye length*, Plasma Phys. Control. Fusion **49** 1193-208 (2007).
- [17] L. Patacchini, I.H. Hutchinson and G. Lapenta, *Electron collection by a negatively charged sphere in a collisionless magnetoplasma*, Phys. Plasmas **14** 062111 (2007).
- [18] L. Patacchini and I.H. Hutchinson *Ion-collecting sphere in a stationary, weakly magnetized plasma with finite shielding length*, Plasma Phys. Control. Fusion **49** 1719-1733 (2007).
- [19] L. Patacchini and I.H. Hutchinson, *Explicit time-reversible orbit integration in Particle In Cell codes with static homogeneous magnetic field*, J. Comp. Phys. **228** 2604-2615 (2009).
- [20] I.H. Hutchinson, *Oblique ion collection in the drift approximation: How magnetized Mach probes really work* Phys. Plasmas **15** 123503 (2008).
- [21] L. Patacchini MSc Thesis: *Collisionless ion collection by a sphere in a weakly magnetized plasma*, MIT, PSFC RR-07-5.
- [22] J.P. Gunn, C. Boucher, P. Devynck *et al*, *Edge flow measurements with Gundestrup probes*, Phys. Plasmas **8**(5) 2001.
- [23] I.H. Hutchinson, *A fluid theory of ion collection by probes in strong magnetic fields with plasma flow*, Phys. Fluids **30**(12) 3777 (1987).
- [24] K-S. Chung and I.H. Huchinson, *Kinetic theory of ion collection by probing objects in flowing strongly magnetized plasmas*, Phys. Rev. A **38**(9) 4721 (1988).